

Revisiting visual-inertial structure from motion for odometry and SLAM initialization

Georgios Evangelidis Branislav Micusik
 Snap Inc.
 Vienna, Austria
 georgios@snap.com brano@snap.com

Abstract—In this paper, an efficient closed-form solution for the state initialization in visual-inertial odometry (VIO) and simultaneous localization and mapping (SLAM) is presented. Unlike the state-of-the-art, we do not derive linear equations from triangulating pairs of point observations. Instead, we build on a direct triangulation of the unknown 3D point paired with each of its observations. We show and validate the high impact of such a simple difference. The resulting linear system has a simpler structure and the solution through analytic elimination only requires solving a 6×6 linear system (or 9×9 when accelerometer bias is included). In addition, all the observations of every scene point are jointly related, thereby leading to a less biased and more robust solution. The proposed formulation attains up to 50 percent decreased velocity and point reconstruction error compared to the standard closed-form solver. Apart from the inherent efficiency, fewer iterations are needed by any further non-linear refinement thanks to better parameter initialization. In this context, we provide the analytic Jacobians for a non-linear optimizer that optionally refines the initial parameters. The superior performance of the proposed solver is established by quantitative comparisons with the state-of-the-art solver.

I. INTRODUCTION

Visual odometry [26] or SLAM [3] solutions, whereby the pose of an agent within an unknown map is tracked, have become a necessity with the advent of autonomous robots and Augmented Reality (AR) wearables that are equipped with cameras. The underlying geometry problem that needs solving is the Structure-from-Motion (SfM) problem that aims at recovering the structure of a scene, as well as the poses of a moving camera, from image correspondences [10].

In principle, visual data would suffice to solve SfM. In practice, however, apart from the scale ambiguity when a monocular sensor is used, the use of scene-dependent visual observation raises accuracy and efficiency issues. This led to the design of mixed sensors that combine visual sensing with other modalities. A successful paradigm is the fusion of visual with inertial data which has been proven to be beneficial for odometry solutions [4]. The integration of inertial data, typically delivered by an Inertial Measurement Unit (IMU), not only provides valuable information for the ego-motion estimation, but it also resolves ambiguities of visual cues (low-texture, fast motion etc).

The resulting visual-inertial odometry (VIO) problem is usually cast into either a filtering formulation [23], [17] or a chain of optimizations [16], [13]. Therefore, the initialization

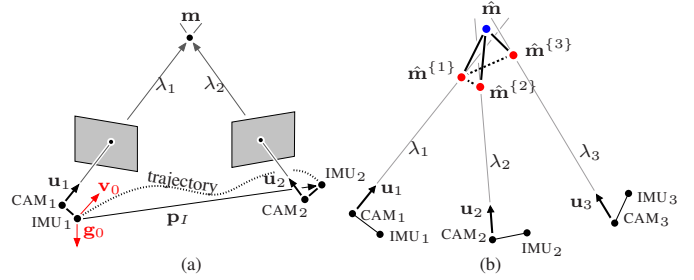


Fig. 1. (a) The *two-view visual-inertial triangulation* principle: the camera baseline is decomposed to the camera-to-IMU distances and to the IMU displacement \mathbf{p}_I that linearly depends on velocity \mathbf{v}_0 and local gravity \mathbf{g}_0 through the kinematic equation. (b) The multi-view case: The total distance between the single reconstruction $\hat{\mathbf{m}}$ and all the candidates $\hat{\mathbf{m}}^{\{i\}}$ (solid lines) is minimized by the proposed solver. Instead, [22] minimizes the distance between the candidate pairs (dashed lines), that is, $\hat{\mathbf{m}}^{\{1\}}$ plays the role of $\hat{\mathbf{m}}$. Only ideal conditions and perfect data make the two formulations equivalent.

of the state is required to either start or recover from divergence. The state typically includes the pose and the velocity of the sensor, while the reconstruction of the map points is implicitly required. When the sensor is strictly static, state initialization reduces into a simple orientation problem using only accelerometer data. However, when the system undergoes motion, the initialization becomes more difficult and visual-inertial SfM (vi-SfM [22]) must be solved. In addition, inexpensive inertial sensors and rolling-shutter cameras make vi-SfM even more challenging due to biased readings and sequential readout, respectively.

Recently, [22] introduced a linear model for vi-SfM that builds on the triangulation principle. We refer here to this principle as *two-view visual-inertial triangulation* (see Fig. 1(a)). The derivation stems from the fact that the camera displacement can be expressed by a kinematic differential equation whereby, under some assumptions, unknown state and auxiliary parameters become linearly dependent. As a result, a closed-form solution for the problem in question becomes feasible.

In this context, we build on the visual-inertial triangulation principle, but in a multi-view sense. More specifically, instead of linking multiple pairs of image observations, we *jointly* relate all the image observations with their generator, that is, the scene 3D point (see Fig. 1(b)). This leads to

a different structure of the linear dependence among state and auxiliary parameters with two main advantages. Firstly, it allows the elimination of auxiliary variables at negligible cost, such that the initial velocity and orientation against the gravity axis can be determined by solving a 6×6 linear system. Secondly, the joint dependence of all the point observations from the single yet unknown map point makes the estimator less biased. As a result, an inherently efficient and robust closed-form solution becomes available. The advantages against the formulation of [22] are discussed in detail in Sec. III. As it is customary, we also combine the proposed solver with a non-linear refinement that better models any underlying non-linearity, such as the dependence on the gyroscope bias [14]. The analytic Jacobians for the non-linear optimization are also provided.

To the best of our knowledge, this is the first work that focuses on the special structure of the resulting linear system. While most prior work solves a large linear system [5], [22], [14], [25], we here show that this is unnecessary. The structure of the proposed system matrix allows for very cheap elimination, and hence, an efficient state initializer. The proposed elimination does not depend on any gravity related constraint that needs to be enforced [22]. Rather, it separates the IMU state from the map points, that is, any constraint can be directly added to the eliminated system.

II. RELATED WORK

While most of the methods assume known initial conditions for VIO [23], [17], there has been no much related work that focuses on the initialization per se.

Provided a calibrated device, the linear dependence of state parameters was discussed in [21], whereby an observability analysis was presented and a closed-form initializer was derived. An extended work, though, that included a simpler closed-form and a thorough resolvability analysis for both biased and unbiased cases was then presented in [22]. The latter constitutes the baseline for later work [14], [2], as well as for our method.

As far as the linear model is concerned, [22] relates corresponding visual observations through the camera baseline, which linearly depends on the unknown state parameters, that is, the velocity, the gravity in the IMU frame and the accelerometer bias. Each visual correspondence contributes three equations, while the distances between map points and the cameras become unknown parameters too. The resulting linear system is then solved, with an optional constraint on the gravity magnitude. The robustness of the method against biased IMU readings was investigated by [14] and, to account for the gyroscope bias, a non-linear refinement method was proposed. The work of [2] then built on [22], [14] and improved the method via multiple loops of visual-inertial bundle adjustments and consensus tests.

The above methods adopt an early fusion approach, a.k.a. tightly-coupled fusion. Instead, visual SfM problem can be first solved and IMU data can be later integrated in a more loosely-coupled framework [15], [25], [12]. In this context, [15] suggested using visual SfM to obtain camera

velocity differences which are then combined with integrated IMU data to recover the scale and gravity direction. The initialization part of [25] used scaleless poses from ORB-SLAM [24] and then solved several sub-problems to initialize the state and the biases along with the absolute scale. This multi-step solution for the parameter initialization was then adapted in [27].

The initialization problem becomes harder when the device is uncalibrated [5], [12]. Even if the biases are known or ignored, the unknown orientation between camera and IMU makes the model non-linear and iterative optimization is necessary. In [5], two solutions to estimate the unknown orientation are proposed, thus allowing solving a linear system that, in turn, initializes a non-linear estimator. Instead, [12] builds on the multi-step approach of [25] to jointly calibrate the extrinsics and initialize the state parameters. In a real scenario, however, the joint solution of calibration and initialization problem using only the very first few frames might make the pose tracking algorithm prone to diverge.

It is worth noting that all the above works silently assume that visual observations come from a global-shutter sensor. Consumer devices, however, are mostly equipped with rolling-shutter cameras. This means that rolling-shutter effects need to be properly handled [11], [18], [1]. Since our test platform is a stereo rolling-shutter rig, we take into account the rolling-shutter readout time when implementing any method in Sec. IV.

III. PROPOSED FORMULATION & SOLUTION

Assume a 3D point \mathbf{m} in a reference coordinate system (RCS) that is observed at N different times by a moving camera via the transformation

$$\lambda_i \mathbf{R}_{C_i} \mathbf{u}_i + \mathbf{p}_{C_i} = \mathbf{m}, \quad i = 1, \dots, N, \quad (1)$$

where \mathbf{u}_i is the normalized (calibrated) unit vector of the underlying image observation, λ_i is the distance between the point and the camera, \mathbf{R}_{C_i} is the rotation from the camera coordinate system (CCS) to the RCS, \mathbf{p}_{C_i} is the camera position in the RCS, at the time $t_i = t(n_i T_s)$, $n_i \in \mathbb{N}$, and T_s is a sufficiently low sampling time. Note that RCS is different than any CCS.

Assume also an intrinsically and extrinsically (against the camera) calibrated IMU that is rigidly mounted to the moving rig.¹ Without loss of generality, the sampling period of the inertial signal can be set to T_s , as shown in Fig. 2. If we now consider the inertial frame at time $t_0 = 0$ as the RCS, the camera position \mathbf{p}_{C_i} can be written as

$$\mathbf{p}_{C_i} = \mathbf{p}_{I_i} + \mathbf{R}_{I_i} \mathbf{p}_C^I, \quad (2)$$

where \mathbf{R}_{I_i} , \mathbf{p}_{I_i} are the rotation and position, respectively, of the IMU in the RCS at time t_i and \mathbf{p}_C^I is the known position of the camera in the inertial frame.

Let us now assume a constant acceleration kinematic model [20] that describes the position of the IMU over

¹We silently assume that both IMU and camera are triggered by a common clock. In practice, a temporal calibrated offset aligns the time axes of the sensors.

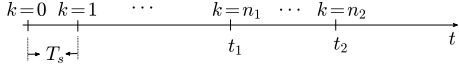


Fig. 2. Sampling times: T_s corresponds to the sampling period of inertial data; timestamps of visual observations, $t_1 = t(n_1 T_s)$ and $t_2 = t(n_2 T_s)$, coincide with irregular inertial sampling times.

time. Provided that $\mathbf{p}_{I_0} = \mathbf{0}$ and \mathbf{v}_0 are the position and velocity, respectively, of the IMU in the RCS at time $t_0 = 0$, the successive integration of acceleration data results in the following equation,

$$\mathbf{p}_{I_i} = t_i \mathbf{v}_0 + \frac{t_i^2}{2} \mathbf{R}_W \mathbf{g}_W + \frac{T_s^2}{2} \sum_{k=0}^{n_i-1} \beta_{ki} R_{I_k} (\boldsymbol{\alpha}_{I_k} + \mathbf{b}_a), \quad (3)$$

where \mathbf{g}_W is the gravity vector in the world coordinate system (WCS), \mathbf{R}_W is the rotation from WCS to the RCS, $\boldsymbol{\alpha}_{I_k}$ is the measured acceleration at time t_k , \mathbf{b}_a is the accelerometer bias that is considered constant for short integration times, and $\beta_{ki} = 2(n_i - k) - 1$ is the resulting coefficient from unfolding recursive integrations.

As mentioned, the IMU is internally calibrated and rigid corrections of gyroscope and accelerometer axes have been pre-applied. However, sensor biases may be affected by several sources and their online refinement is recommended. As seen, the accelerometer bias offset \mathbf{b}_a can be added in a linear way. However, a gyroscope bias offset would break the linearity and its use through a non-linear refinement, when needed, is preferred [14], [2]. Assuming now that the bias has been removed, any rotation R_{I_i} can be computed from integrating gyroscope data [20],

$$R_{I_i} = \prod_{k=0}^{n_i-1} \exp(\boldsymbol{\omega}_k T_s) = \exp(\boldsymbol{\omega}_0 T_s) \dots \exp(\boldsymbol{\omega}_{i-1} T_s) \quad (4)$$

where $\boldsymbol{\omega}_k$ is the gyroscope measurement. As a result, \mathbf{R}_{C_i} can be as well estimated using the known orientation of the CCS in the IMU frame $\mathbf{R}_{C_i}^I$, that is, $\mathbf{R}_{C_i} = \mathbf{R}_{I_i} \mathbf{R}_{C_i}^I$.

The equations (1), (2) and (3) can be combined into a single matrix form as

$$\begin{bmatrix} t_i \mathbf{I}_3 & \frac{t_i^2}{2} \mathbf{I}_3 & \mathbf{B}_i & -\mathbf{I}_3 & \mathbf{R}_{C_i} \mathbf{u}_i \end{bmatrix} \begin{bmatrix} \mathbf{v}_0 \\ \mathbf{g}_0 \\ \mathbf{b}_a \\ \mathbf{m} \\ \lambda_i \end{bmatrix} = \mathbf{c}_i, \quad (5)$$

where $\mathbf{g}_0 = \mathbf{R}_W \mathbf{g}_W$ is the gravity in the RCS, $\mathbf{c}_i = -\mathbf{R}_{I_i} \mathbf{p}_I^C - \frac{T_s^2}{2} \sum_{k=0}^{n_i-1} \beta_{ki} R_{I_k} \boldsymbol{\alpha}_{I_k}$ is a constant vector that includes accumulation of weighted and rotated acceleration measurements, $\mathbf{B}_i = \frac{T_s^2}{2} \sum_{k=0}^{n_i-1} \beta_{ki} R_{I_k}$ is a weighted sum of rotation matrices, and \mathbf{I}_3 is the 3×3 identity matrix.

Since N observations of the point \mathbf{m} are available, one can easily extend the above linear equations system. Any new observation contributes three equations while adding one unknown λ parameter, thus shaping a linear system of $3N \times (N + 12)$ size. In principle, a single 3D point with 6 observations would suffice to solve for all the unknowns. However, such a problem would be ill-conditioned and in

practice several 3D points along with their observations must be used.

Recall that the goal of the initialization is to estimate the initial velocity \mathbf{v}_0 and the orientation \mathbf{R}_W . Given that $\mathbf{g}_W = [0, 0, \gamma]^T$ with γ being the gravity magnitude, \mathbf{g}_0 constitutes a scaled version of the third column of \mathbf{R}_W . As a result, any rotation around the world gravity axis is not identifiable and \mathbf{R}_W is estimated up to this unknown angle. Note also that \mathbf{b}_a is not separable from \mathbf{g}_0 unless the system rotates, that is, $\mathbf{R}_{I_k} \neq \mathbf{I}_3$.²In this case, a constraint $\|\mathbf{g}_0\|_2 = \gamma$ can optionally be enforced.

A. Closed-form solution

Unlike [22], we do not relate observation pairs. Instead, we add the unknown points, expressed in the RCS, into the parameter vector and directly relate every single point with its observations, that is, \mathbf{m} remains an unknown parameter of the linear system. Such an approach may initially result in an unknown vector of slightly higher dimension. However, as we see below, the matrix of the linear system has a simpler form and any elimination can be obtained at no cost, that is, without any matrix inversion or decomposition. Moreover, the direct reconstruction of the points in the RCS comes as a by-product.

Let us consider M map points $\mathbf{m}_j, j = 1, \dots, M$ and let λ_{ji} and \mathbf{u}_{ji} denote the corresponding rays and distances, respectively. For the sake of simplicity, we assume that each point has the same number of N observations (captured at N different times) while in practice each point can have a different number of observations. Then, the entire linear system can be written as

$$[\mathbf{V} \mid \mathbf{W} \mid \mathbf{Q}] \begin{bmatrix} \mathbf{v}_0 \\ \mathbf{g}_0 \\ \mathbf{b}_a \\ \mathbf{m}_1 \\ \vdots \\ \mathbf{m}_M \\ \lambda_{1i} \\ \dots \\ \lambda_{MN} \end{bmatrix} = \mathbf{c}, \quad (6)$$

where \mathbf{V} is a $3MN \times 9$ matrix, \mathbf{W} is a $3MN \times 3M$ block matrix, \mathbf{Q} is a $3MN \times MN$ block matrix and \mathbf{c} is a constant vector of length $3MN$:

$$\mathbf{V} = \begin{bmatrix} t_{11} \mathbf{I}_3 & \frac{t_{11}^2}{2} \mathbf{I}_3 & \mathbf{B}_{11} \\ \vdots & \vdots & \vdots \\ t_{MN} \mathbf{I}_3 & \frac{t_{MN}^2}{2} \mathbf{I}_3 & \mathbf{B}_{MN} \end{bmatrix}, \quad (7)$$

$$\mathbf{W} = \begin{bmatrix} \mathbf{Y}_1 & & \\ & \ddots & \\ & & \mathbf{Y}_M \end{bmatrix}, \quad (8)$$

²When $\mathbf{R}_{I_k} = \mathbf{I}_3$ then $\mathbf{B}_i = \frac{t_i^2}{2} \mathbf{I}_3$ which is equal to the coefficient of \mathbf{g}_0 .

$$\mathbf{Q} = \begin{bmatrix} \mathbf{q}_{11} & & \\ & \ddots & \\ & & \mathbf{q}_{MN} \end{bmatrix}, \quad (9)$$

$$\mathbf{c} = \begin{bmatrix} \mathbf{c}_{11} \\ \vdots \\ \mathbf{c}_{MN} \end{bmatrix} \quad (10)$$

with $\mathbf{Y}_j = -[\mathbf{I}_3, \dots, \mathbf{I}_3]^\top$ being a $3N \times 3$ block and $\mathbf{q}_{ji} = \mathbf{R}_{C_{ji}} \mathbf{u}_{ji}$.

However, λ 's are auxiliary variables and their elimination is meaningful. Commonly, one would multiply by left with the projection matrix $\mathbf{P} = \mathbf{I} - \mathbf{Q}(\mathbf{Q}^\top \mathbf{Q})^{-1} \mathbf{Q}^\top$.³ Recall, however, that each block of \mathbf{Q} is a unit vector, hence $(\mathbf{Q}^\top \mathbf{Q})^{-1} = \mathbf{I}$. As a consequence, the block diagonal matrix $\mathbf{P} = \mathbf{I} - \mathbf{Q}\mathbf{Q}^\top$ can be computed without any inversion and such an elimination comes at negligible cost. The system one needs to initially construct is the following:

$$[\mathbf{P}\mathbf{V} \mid \mathbf{P}\mathbf{W}] \begin{bmatrix} \mathbf{v}_0 \\ \mathbf{g}_0 \\ \mathbf{b}_a \\ \mathbf{m}_1 \\ \vdots \\ \mathbf{m}_M \end{bmatrix} = \mathbf{P}\mathbf{c} \quad (11)$$

It now becomes evident that the linear system is smaller than the one of [22], [14] since $M \ll MN$. Note that homogeneous equations that relate pairs of λ -based reconstructed points are added in the linear system of [22], thereby increasing the number of rows. We do not add such constraints here since all the image observations of a single point are *jointly* related through a single unknown parameter.

We now proceed with a second elimination step that further reduces the above linear system into one that only solves for the IMU state. One can optionally back-substitute to compute the points, when needed. To this end, we apply the projection operator $\mathbf{I} - \mathbf{P}\mathbf{H}\mathbf{W}^\top \mathbf{P}^\top$, where $\mathbf{H} = (\mathbf{W}^\top \mathbf{P}\mathbf{W})^{-1}$ since \mathbf{P} is symmetric and idempotent. However, it is straightforward to show that $\mathbf{W}^\top \mathbf{P}\mathbf{W}$ is a block diagonal matrix of size $3M \times 3M$, with each block being defined by $N(\mathbf{I}_3 - \frac{1}{N} \sum_{i=1}^N \mathbf{q}_{ji} \mathbf{q}_{ji}^\top)$. Hence, the computation of \mathbf{H} requires inverting each 3×3 block, which is given by a simple analytical formula. Alternatively, one could make use of the Sherman-Morrison formula [9] for an inversion-free recursive computation with rank-1 updates.

The elimination of map points finally leads to the following minimal system

$$[\mathbf{P}\mathbf{G}\mathbf{V}] \begin{bmatrix} \mathbf{v}_0 \\ \mathbf{g}_0 \\ \mathbf{b}_a \end{bmatrix} = \mathbf{P}\mathbf{G}\mathbf{c} \quad (12)$$

where $\mathbf{P} = \mathbf{I} - \mathbf{Q}\mathbf{Q}^\top$ and $\mathbf{G} = \mathbf{I} - \mathbf{H}\mathbf{W}^\top \mathbf{P}$. Apart from the fact that \mathbf{P} is a block diagonal matrix, the computation of $\mathbf{H}\mathbf{W}^\top$

³This is equivalent to using Schur complement of the matrix $[\mathbf{v} \mid \mathbf{w} \mid \mathbf{q}]^\top [\mathbf{v} \mid \mathbf{w} \mid \mathbf{q}]$.

from \mathbf{H} involves only additions since all blocks of \mathbf{W} are identity matrices. As a consequence, we end up with a 9×9 , or a 6×6 in the unbiased case, linear system that can be very efficiently built. Still, the norm equality constraint $\|\mathbf{g}_0\|_2 = \gamma$ can be optionally added. There are several options to solve the resulting constrained problem, e.g., solving the unconstrained linear system followed by a one-step refiner, adding a quadratic constraint in a convex optimization framework, or applying QR decomposition to name a few. Additionally, any weighting scheme per observation or per map point easily applies.

When the point reconstruction is required, one can use the following equation to compute the coordinates:

$$\begin{bmatrix} \mathbf{m}_1 \\ \vdots \\ \mathbf{m}_M \end{bmatrix} = \mathbf{H}\mathbf{W}^\top \mathbf{P}(\mathbf{c} - \mathbf{V}\mathbf{z}^*) \quad (13)$$

where $\mathbf{z}^* = [\mathbf{v}_0^*, \mathbf{g}_0^*, \mathbf{b}_a^*]^\top$ is the solution of (12).

Finally, the rotation matrix \mathbf{R}_W is computed from the angle between the vectors \mathbf{g}_0 and \mathbf{g}_W , while \mathbf{v}_0 and \mathbf{m}_j are expressed in the WCS by $\mathbf{R}_W^\top \mathbf{v}_0$ and $\mathbf{R}_W^\top \mathbf{m}_j$, respectively. Since the origin of the WCS can be arbitrarily chosen, it can be identified with the origin of the RCS.

We summarize below the advantages of the above linear solver compared to [22], [14]:

- The linear system has an inherently simpler structure and is eliminated at negligible cost. This leads to a more efficient solution that only requires inverting or decomposing a very small matrix.⁴ The elimination of λ 's in [22], [14] would require inverting or decomposing a large sparse matrix with more complicated structure.
- The proposed formulation leads to a linear system with uniquely defined structure. In contrast, the structure of the linear system of [22] depends on how the observations pairs are combined and on how the points appear in frames. Note that, in practice, each point appears at different frames.
- The reconstruction of the map points in a single RCS is directly obtained by the linear solver. When requested, it is the linear solver that directly estimates their coordinates. In [22], [14], one would typically average the many putative reconstructions per point, or choose the reconstruction in one of the CCS, while different points are reconstructed in different CCS.
- The estimation is better conditioned since all the point observations are jointly and symmetrically related through the single yet unknown point that generates them.
- The model naturally extends to a bundle adjustment scheme with the same parameters, e.g. by applying a projection operator. Instead, initial map points in a single RCS or CCS should be pre-computed when the solver of [22], [14] is used.

⁴When the bias is ignored, the solution can be easily derived analytically using the Woodbury identity, thus avoiding any matrix decomposition, or matrix inversion algorithm.

Note that, apart from the difference in computational complexity, the two solvers provide different solutions. Only *ideal conditions* and *perfect data* would make the two solvers provide same solutions.

Rolling-shutter vs. global-shutter camera: As is well known, global shutter cameras adopt a single exposure-then-readout step for the whole image. Rolling shutter cameras, though, have a multi-step mechanism that captures the image rows sequentially, at different times. We deliberately refer to the time index in (1) to consolidate these two cases. Simply, all the visual observations of a single image have the same timestamp in global shutter mode. Instead, the timestamp of a visual observation of a rolling-shutter image can be given by $t_i = \tau_i + \tilde{u}_i^y \Delta\tau$, where τ_i is the timestamp of the first image row, \tilde{u}_i^y is the lens-distorted y-coordinate (image row) of the projection of \mathbf{m} on the image and $\Delta\tau$ is the readout time per image row. As a result, \mathbf{R}_{I_i} and \mathbf{p}_{I_i} vary across a rolling shutter image. In practice, when t_i falls between two IMU sampling times, an interpolation scheme is employed.

Monocular vs. Binocular sensor:: So far, we have not referred to a particular type of camera, namely a monocular or binocular camera, since the model is valid with either type (recall that \mathbf{m} is expressed in RCS and \mathbf{u}_i may regard any frame of a binocular sensor). What may be different though is the integration time needed to reliably initialize the state, because the observability grows with the number of images, hence with the number of sensors. To be more specific, the stereo baseline leads to larger camera displacements, which in turn leads to better triangulation. For instance, given two successive stereo frames, the displacement from the *current left* to the *next left* camera is most of the times smaller than the distance between the *current left* and the *next right* camera. The epipolar constraint on a *single stereo frame* does not explicitly contribute to the problem in question, since the integration time is roughly the same for conjugate image points. It may be though a strong constraint for the tracking problem per se, that is, multiple visual correspondences that feed the initializer can be more reliable when multi-view constraints are enabled. Overall, provided that motion singularities nicely presented in [22] are not met, one should expect higher integration times when switching from stereo to monocular camera in order to reliably solve the problem.

B. Non-linear refinement

The underlying application may require high accuracy while the available hardware may support computationally demanding operations. Therefore, we suggest a further refinement of the IMU state and the reconstructed points in an iterative optimization framework. We do not solve a multi-keyframe Visual-Inertial Bundle Adjustment problem whereby multiple states are optimized [2]. Instead, we just optimize the image reprojection error *w.r.t.* the parameters of the minimal solver, that is, the initial velocity along with the rotated gravity vector, and optionally the sensor biases.

As seen in Fig. 1, the solver in (12) minimizes the distance between 3D vectors. Despite the geometric nature, the fact that both 3D vectors are assigned unknown parameters

may give unwanted freedom to the solver. Therefore, the projection of the error distance onto a manifold (surface) where one of the two vectors remains constant is more meaningful (λ disappears after projection). Commonly, the image itself or the calibrated image plane at $z = 1$ of the CCS is used.

Let us denote the total error that needs minimizing as

$$f(\mathbf{x}) = \sum_{i,j} d_{ij} (\pi(\mathbf{R}_{C_i}^\top \mathbf{m}_j - \mathbf{R}_{C_i}^\top \mathbf{p}_{C_i}), \pi(\mathbf{u}_{ji})) \quad (14)$$

where $\mathbf{x} = [\mathbf{v}_0^\top, \mathbf{g}_0^\top, \mathbf{b}_a^\top, \mathbf{m}_1^\top, \dots, \mathbf{m}_{M1}^\top]^\top$, d_{ij} is a Euclidean distance and $\pi(\mathbf{u}) = [u_x/u_z, u_y/u_z]^\top$ is the common perspective projection.

To avoid a constrained optimization when the equality constraint $\|\mathbf{g}_0\|_2 = \gamma$ must be enforced, we model the local gravity as a rotated version of world gravity, that is,

$$\mathbf{g}_0 = \gamma \begin{bmatrix} \frac{\sin(\|\phi\|)}{\|\phi\|} \phi_y \\ -\frac{\sin(\|\phi\|)}{\|\phi\|} \phi_x \\ \cos(\|\phi\|) \end{bmatrix} \quad (15)$$

where $\phi = [\phi_x, \phi_y, 0]^\top$ is the angle-axis representation of \mathbf{R}_{W} . Recall that modelling the rotation around the gravity axis is meaningless.

The gyroscope bias can be also inserted into the model in a non-linear way [8]. In such a case, the unknown vector \mathbf{x} is augmented by an extra parameter \mathbf{b}_g . We model the gyroscope bias in the experimental section to evaluate its contribution into the parameter estimation.

We employ a Levenberg-Marquardt framework to minimize $f(\mathbf{x})$, similar to the one used for bundle adjustment [19]. The Jacobians of the linearized form of $f(\mathbf{x})$ with respect to the parameters (including the gyroscope bias) are given in the Appendix A.

IV. EXPERIMENTS

A. Experimental setup

We are interested in experimenting with a stereo rolling shutter (RS) camera rigged with an IMU. In order to get realistic data with ground truth (GT) structure and poses, we process data from Snap Spectacles. States resulting from a Kalman filter on visual-inertial data play the role of GT states and high-order splines on IMU data provide ideal gyroscope and acceleration readings, such that a continuous integrator perfectly interpolates between the filter states. IMU data are then sampled at 800Hz and finally, noise and time varying biases are added based on the calibrated variances of the used device.

A virtual stereo rolling shutter camera of VGA resolution follows the resulting trajectory within a virtual 3D scene and images are rendered at 30Hz.⁵ When GT image correspondences are needed, single virtual 3D points along with their reprojections are created. Given a reference image, we back-project 100 evenly spaced image points with random depth in range [1m, 15m] and the points are in turn re-projected into

⁵Unreal Engine is used [6].

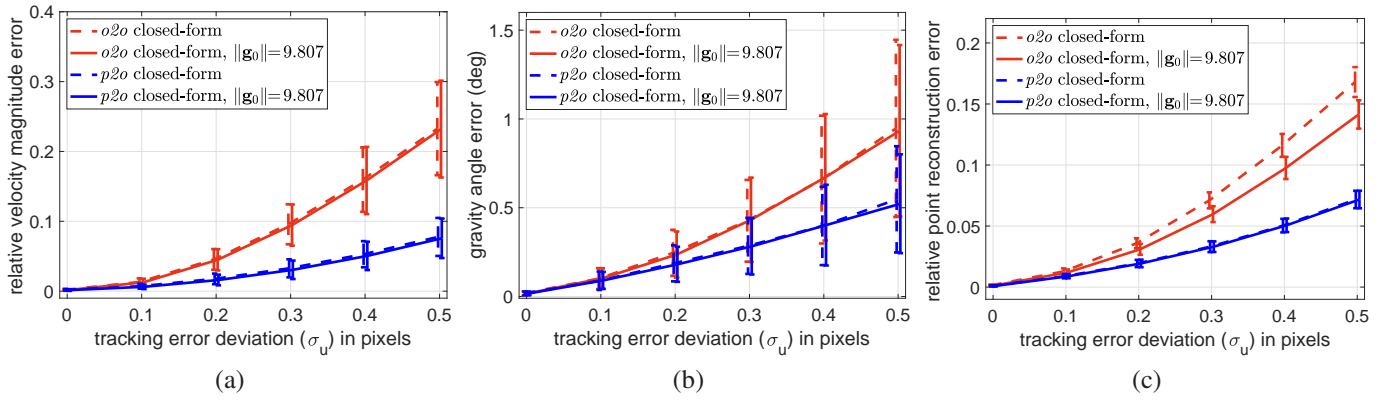


Fig. 3. (a) Velocity estimation, (b) gravity orientation estimation and (c) point reconstruction error as a function of point tracking error; the integration time is 0.46 seconds ($N_f = 3$).

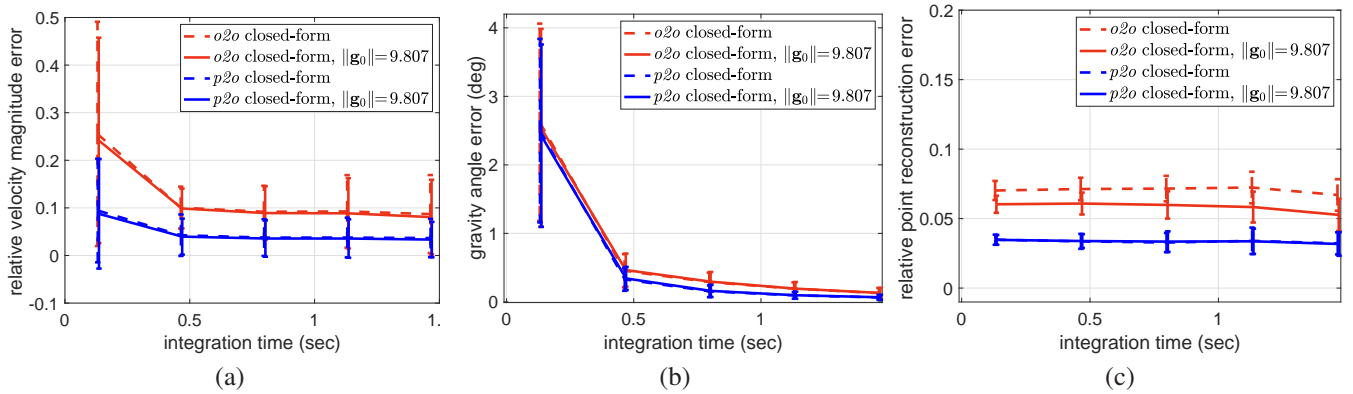


Fig. 4. (a) Velocity estimation, (b) gravity orientation estimation and (c) point reconstruction error as as function of integration time; the point tracking error deviation is 0.3 pixels.

adjacent frames. To get real correspondences from rendered images, an ECC-based tracker [7] on FAST corners [28] is employed, while a RANSAC-based scheme removes strong outliers. The tracked features do not necessarily appear in any frame of the time window. We here consider tracks from 5 stereo frames, but we modify the frame upsampling factor to change the integration time and the rig displacement.

Note that that the sequential readout of a RS camera implies multiple different pose instances even when considering a window of a few frames. As a consequence, the singular cases due to a very small number of frames [22] are not met here. In addition, the stereo camera makes the parameters observable within short time intervals.

B. Closed-form performance evaluation

We compare the performance of the proposed solver against the solver of [22]. We do not consider biases here and we deal with them below when non-linear refinement is employed. We refer to the proposed solver as *point-to-observation* (*p2o*) pairing scheme as opposed to *observation-to-observation* (*o2o*) pairing paradigm of [22], [14].

We use data from a sequence where a Snap Spectacles wearer is almost static for about 1 second and s/he then walks forward for 12 seconds while looking around. Such a sequence mixes translational and rotational movements while it includes instant stationary parts. We here use virtual points

and the tracks of GT image observations that are affected by additive Gaussian noise of known deviation σ_u .

First, we test the robustness of the solvers in terms of the tracking error, which found to be the dominant parameter that affects the performance. For each value of σ_u in the range $[0, 0.5]$ pixel, a sliding window of 5 temporarily upsampled frames is used. The upsampling factor is $N_f = 3$, thus defining a total integration time of 0.46s. Any frame window with GT velocity magnitude below 0.01m/s is discarded. In total, 50 realizations per window are executed. The *relative* magnitude error and the angular error are the evaluation criteria used to quantify the velocity and gravity direction estimation, respectively. As for the point reconstruction error, the error distance per point is normalized by its depth. The average error as a function of σ_u , with and without the gravity norm constraint, is shown in Fig. 3. As seen, the proposed *p2o* formulation is more robust and provides more accurate estimations, while its superiority against *o2o* formulation grows with the tracking error. When the gravity norm constraint is enforced, the performance improvement is not noticeable in most of the cases.

Next, we investigate how the integration time affects the performance. Recall here that the goal is to initialize the state reliably and as fast as possible. We repeat the experiment with $\sigma_u = 0.3$ and test several upsampling factors N_f from

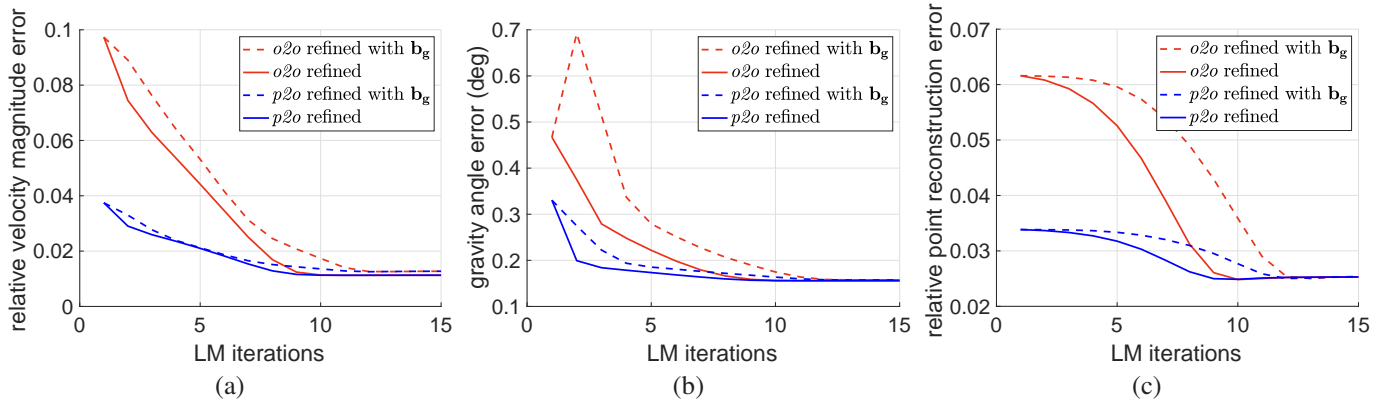


Fig. 5. (a) Velocity estimation, (b) gravity orientation estimation and (c) point reconstruction error attained per iteration with non-linear refinement; the point tracking error deviation is 0.3 pixels and the integration time is 0.46 seconds.

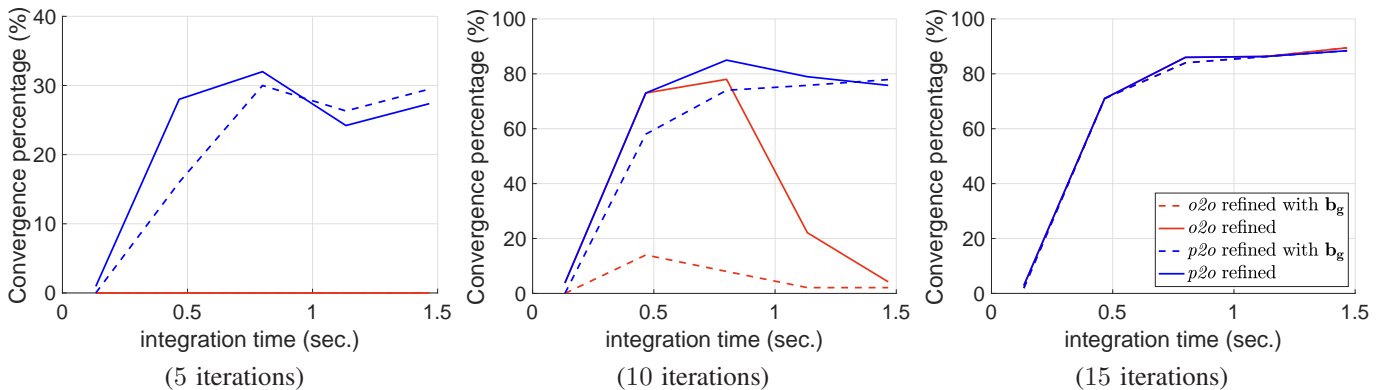


Fig. 6. Frequency of convergence for non-linear refinement as function of integration time when (a) 5, (b) 10 and (c) 15 iterations are allowed.

1 to 9, which implies the integration time range [0.13, 1.46] seconds. Fig. 4 shows the error as a function of integration time. As expected, the shorter the integration time is, the more sensitive the solvers are. The angle error of gravity estimation, in particular, can reach 3 degrees at very short integration times. However, it seems that the solvers provide acceptable results after 0.5 seconds. The proposed solver outperforms and achieves more accurate estimation at any integration time. While the gravity estimation is slightly better, the velocity and the point reconstruction error is decreased by 50% across the whole tested range. Again, the benefit from enforcing the norm equality constraint on gravity vector is minor. It is noted that one should expect higher integration times when monocular camera is used. We experimentally found here that acceptable estimations are obtained after 1.5s with a monocular sensor.

The comparison of timings is meaningless since [22], [14] either invert or decompose a large matrix (e.g. with SVD). Instead, we solve a 6×6 linear system. As a result, there is a substantial gain from replacing *o2o* with *p2o* even when the performance is comparable.

As verified by [14], the accelerometer bias, when separable from the gravity, does not affect the closed-form solution. Rather, the gyroscope bias does affect the performance, when

its magnitude is relatively large and the integration time is long. We reached similar conclusions for both solvers. Therefore, we model the gyroscope bias along with the non-linear refinement in the next experiment.

C. Refinement performance evaluation

We here evaluate the contribution of the closed-form solvers to the non-linear refinement. Our reference is the refiner discussed in Sec. III-B that minimizes the re-projection error. The rotated gravity vector is modelled by (15) and the gyroscope bias is optionally modelled. To initialize the structure when *o2o* solver is used, we average the λ -based reconstructions per point. The analytic Jacobians needed for the optimization are given in Appendix A.

As mentioned, the Levenberg-Marquardt framework is employed for minimization [19]. We do not enable any robust loss since strong outliers do not exist here. We also want to evaluate the net performance of the minimizer. All the thresholds of the stop criteria in [19] are set to 10^{-9} and we let the algorithm terminate.

Fig. 5 shows the error of algorithms per iteration, for the case of $N_f = 3$ and $\sigma_u = 0.3$, averaged over all the realizations and tested frame windows of the sequence. We first confirm the contribution of the new linear solver accuracy and its ability to initialize a minimizer. Notably,

TABLE I
COMPARISON OF AVERAGE PERFORMANCE PER SEQUENCE; .

	WALKING vel.(%)/grav.(deg.)	RUNNING vel.(%)/grav.(deg.)	HEADMOVING vel.(%)/grav.(deg.)
<i>o2o</i> closed-form	2.98% / 0.147°	5.01% / 0.607°	9.82% / 0.216°
<i>p2o</i> closed-form	2.76% / 0.143°	2.42 / 0.339°	6.52% / 0.205°
<i>o2o</i> refined	2.77% / 0.141°	<u>0.45% / 0.145°</u>	5.40% / 0.164°
<i>p2o</i> refined	2.77% / 0.140°	<u>0.45% / 0.145°</u>	5.40% / 0.163°
<i>o2o</i> refined (Cauchy loss)	2.72% / <u>0.124°</u>	2.96% / 0.313°	4.77% / 0.149°
<i>p2o</i> refined (Cauchy loss)	2.71% / 0.125°	0.62% / 0.166°	<u>4.76% / 0.148°</u>
VIO (Kalman filter)	3.05% / 0.099°	3.84%/0.258°	4.85% / 0.151°

boldface: best closed-form solution, underlined: best refinement

when starting from *o2o* solution, more than five iterations are needed to just reach the accuracy of the *p2o* solver. As a result, similar accuracy can be achieved with much less operations. All the counterparts reach almost comparable floor values after 12 iterations which implies a locally convex error function. When the gyroscope bias is modelled and estimated, further non-linearities are introduced and the convergence may be slower. It is noted that the rate of convergence remained unaffected after adjusting the initial damping factor.

We also compare the minimizers in terms of the frequency of convergence. In a real scenario, one would allow a few iterations while he would be more interested in IMU state initialization (the points may be re-triangulated after initialization). Therefore, we consider that the algorithm has converged after a predefined number of iterations when the relative velocity error is below 0.025 and the angular error is below 0.25 degrees. Then, we use this criterion to count the successful realizations for a specific number of iterations. Fig. 6 shows the percentage of convergence as a function of integration time for 5, 10 and 15 iterations. Unlike *p2o* solver, the *o2o* solver would most likely fail to well initialize the state unless a sufficient number of iteration is allowed. We noticed that the vast majority of Levenberg-Marquardt iterations includes a single cost-function evaluation.

The experimental results on artificial data complement the advantages of the proposed formulation. Provided that the new solver is inherently more efficient, it suggests a better method to initialize the state of VIO and SLAM algorithms, either as a minimal solver or combined with non-linear optimization. It is to be noted that the Jacobians of the parameters can be used to estimate the parameter covariances as well [10].

Although the current IMU readings include a time varying accelerometer and gyroscope bias, we did not observe any improvement due to their modelling. This is most likely because of the low noise levels of the used device compared to the dominant tracking error. We experimentally confirmed the ability of the algorithms to estimate high yet unrealistic biases that were artificially added. However, when a refiner is employed, one could ignore the estimation of the biases along with the minimal solver and let only the refiner estimate their values. When time is critical and the biases

are modelled and optimized by a state tracker, one might prefer ignoring bias estimation at the initialization stage.

D. Real correspondences

Different trajectories and types of motion are here combined with different 3D scenes. In all the sequences, the rig is static at the beginning. A rotation-aware ECC-based tracker on FAST corners tracks a maximum number of 200 points per rendered image. As a reference baseline, a well initialized extended Kalman filter that propagates IMU states using visual and inertial data is also employed [23]. The initial static part allows a reliable initialization from accelerometer data. Again, 5 upsampled frames with $N_f = 3$ are used per frame window. To compensate for mismatches and non-Gaussian tracking error, a Cauchy loss [10] in (14) is also tested. A maximum number of 15 iterations for the refinement is allowed.

We test the algorithms on three sequences, WALKING, HEADMOVING and RUNNING. Table I summarizes the error per sequence. The average error over all frame windows per sequence is computed. Overall, the *p2o* solver obtains better estimates than the *o2o* solver. When a non-linear refiner follows, the error further decreases. Fig. 7 shows the error over time per sequence. The absolute velocity magnitude error is here shown instead, and the maximum velocity is also given. Interestingly, the velocity estimation of the closed-form is comparable with the one from Kalman filter for the WALKING and HEADMOVING sequence. However, VIO benefits from the accurate initialization and provides better direction estimates of the local gravity. The RUNNING sequence is more challenging because of jumping while jogging. The proposed solver combined with the refiner clearly outperforms in this case.

E. Real data

The above experimental setup regards rendered image sequences from artificial 3D scenes. We here focus on the the closed-form solvers and test them on two real sequences acquired from Snap Spectacles in a typical open office space. The first sequence, named OFFICELOOP, regards a 25m loop-shaped walking sequence within the office. The second sequence, named LOOKINGAROUND, is more challenging and regards rotational motion with strong velocity variation where the wearer looks around without stepping. In both

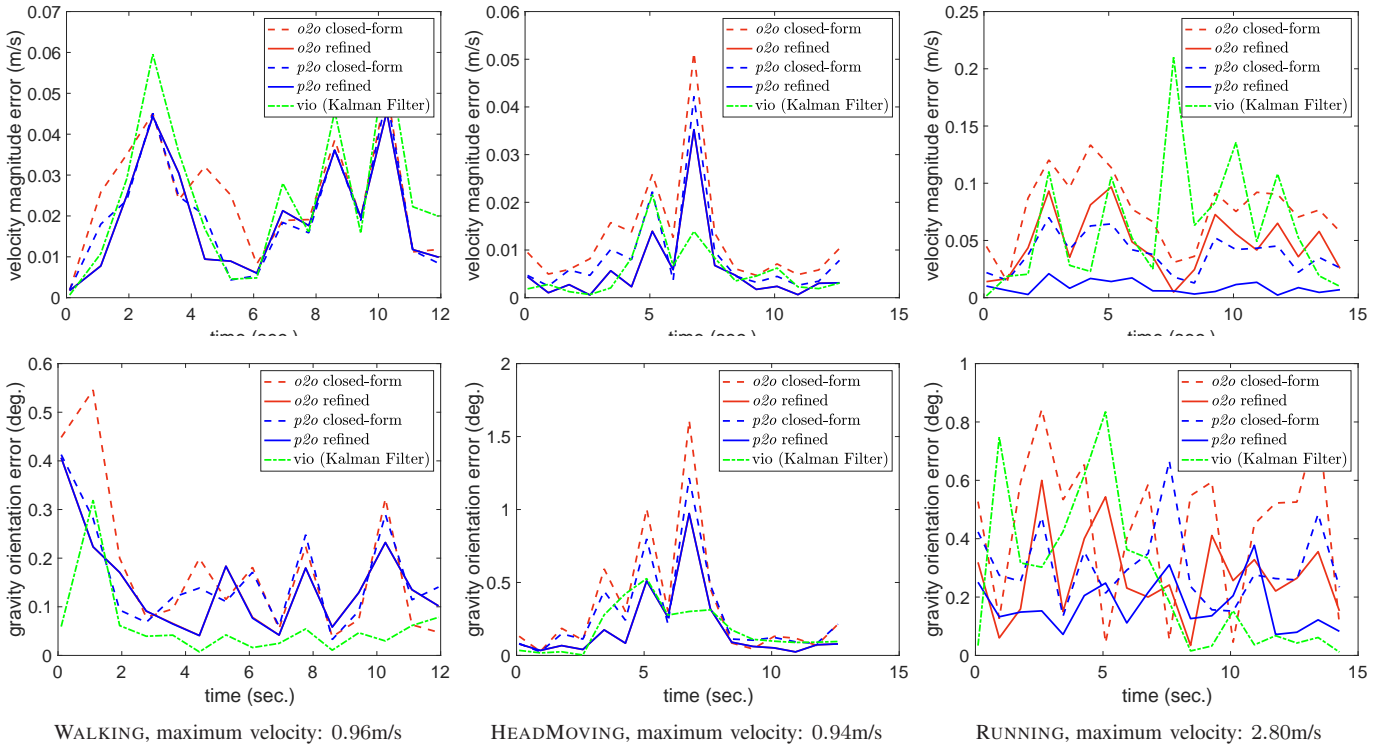


Fig. 7. (top) Velocity and (bottom) gravity orientation error per frame; point correspondences are delivered by a feature tracker on rendered images; the integration time is 0.46s.

cases, the wearer is static in the beginning as well as in the end of the recording.

We employ the minimal solvers and re-initialize the state of every frame using a moving 7-frame window of upsampled frames ($N_f = 3$). Since the ground truth is not available, we show the deviation from the VIO baseline which uses prior information for the state estimation. The velocity and orientation differences are shown in Fig. 8. Although the two solvers provide similar gravity orientations, the velocity estimations are quite different. Unlike the proposed $p2o$ solver, the velocity estimations of the $o2o$ solver are quite far from VIO velocities. As expected, the estimations for the LOOKINGAROUND sequence are worse due to the rapid velocity and rotation changes, which in turn make the feature tracking break more often.

V. CONCLUSIONS

We revisited the vi-SfM problem which is solved by VIO or SLAM methods for state initialization. In this context, we reformulated a widely used linear model and we suggested a new closed-form solution with a twofold advantage. Firstly, the new solver is more efficient because the proposed model allows for elimination at negligible cost, thus leading to a very compact linear system. Secondly, the new formulation leads to a more symmetric and unbiased solution that equally handles the multiple observations of any map point. We also presented a non-linear optimizer that refines the parameters and we provided the analytic Jacobians. The superiority of the proposed closed-form solution against the state-of-the-art, as well as its contribution to the non-linear refinement,

was validated with VIO initialization tests on both artificial and real visual-inertial data from Snap Spectacles.

APPENDIX

A. Jacobians

In this section, we provide the analytic Jacobians for the minimization of $f(\mathbf{x})$ in (14). For the sake of simplicity, we assume a squared Euclidean distance d_{ij} , and a single point \mathbf{m} to skip the index j . Recall the importance of index i when multiple points are used with a rolling-shutter camera, that is, each observation is captured at different time, and under different camera pose.

Suppose a state parameter vector \mathbf{x} obtained from the closed-form solution. The goal of the refiner is to find a correction $\Delta\mathbf{x}$ such that $f(\mathbf{x} + \Delta\mathbf{x}) < f(\mathbf{x})$. If we express the reconstructed point at the camera of the i -th timestamp as $\mathbf{w}_i = \mathbf{R}_{C_i}^\top \mathbf{m} - \mathbf{R}_{C_i}^\top \mathbf{p}_{C_i}$, the linearized problem is written as

$$\min_{\Delta\mathbf{x}} \sum_i \|\pi(\mathbf{w}_i) - \pi(\mathbf{u}_i) + \mathbf{J}_i \Delta\mathbf{x}\|^2 \quad (16)$$

where \mathbf{J}_i is the Jacobian of $\pi(\mathbf{w}_i)$ w.r.t. the state parameters \mathbf{x} . Note that in the general case of multiple points ($\mathbf{m}_j, j = 1, \dots, M$), \mathbf{J}_i is replaced by \mathbf{J}_{ji} , which is a $2 \times (12 + 3M)$ sparse matrix with $(4+M)$ blocks of size 2×3 . When gravity is modelled by (15), \mathbf{J}_{ji} is of size $2 \times (11 + 3M)$ and the gravity Jacobian block has size 2×2 . Only the first four blocks as well the $(4+j)$ -th block have non-zero elements per observation.

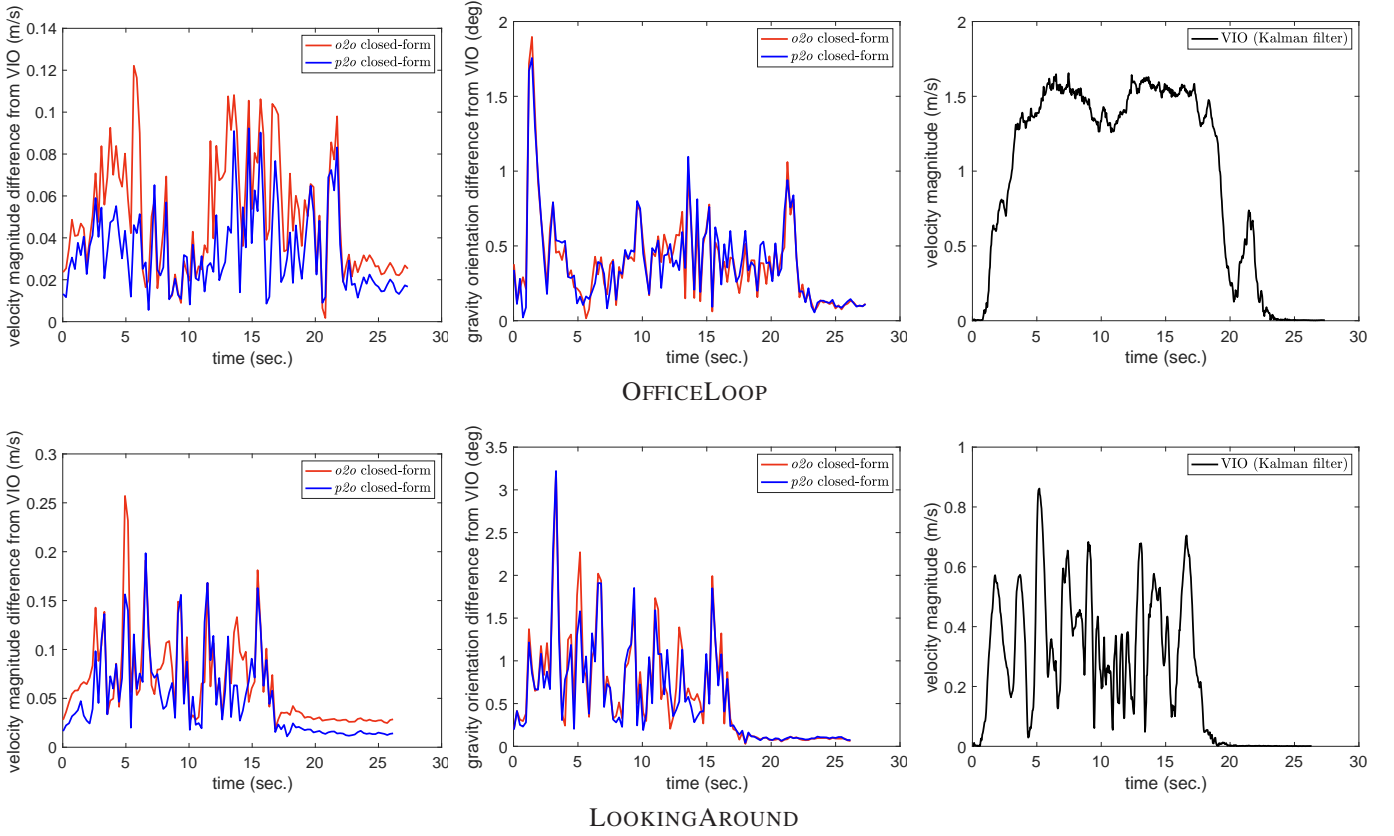


Fig. 8. (left) Velocity and (middle) gravity orientation difference from VIO (VIO velocity is shown on the right side) after testing the minimal solvers on real data delivered by Snap Spectacles.

We below provide the five blocks of the Jacobian J_i . All the blocks include the Jacobian J_π of the projection operator $\pi(\mathbf{w}_i)$. If we assume a 3D vector $\mathbf{w}_i = [x_i, y_i, z_i]^\top$ and the projection operator $\pi(\mathbf{w}_i) = [x_i/z_i, y_i/z_i]^\top$, its Jacobian is given by

$$J_\pi = \frac{1}{z_i} \begin{bmatrix} \mathbf{I}_2 & -\pi(\mathbf{w}_i) \end{bmatrix}. \quad (17)$$

The first block of J_i regards the velocity and is given by:

$$\frac{\partial \mathbf{w}_i}{\partial \mathbf{v}_0} = -t_i J_\pi \mathbf{R}_{C_i}^\top \quad (18)$$

The second block of J_i regards the gravity and in case that the norm constraint is not enforced is simply given by :

$$\frac{\partial \mathbf{w}_i}{\partial \mathbf{g}_0} = -\frac{t_i^2}{2} J_\pi \mathbf{R}_{C_i}^\top. \quad (19)$$

When the gravity is modelled by (15), this block becomes 2×2 and the two columns are given by

$$\frac{\partial \mathbf{w}_i}{\partial \phi_x} = \frac{\partial \mathbf{w}_i}{\partial \mathbf{g}_0} \left(\gamma_c \begin{bmatrix} \phi_x \phi_y \\ -\phi_x^2 \\ 0 \end{bmatrix} + \gamma_s \begin{bmatrix} -\phi_x \phi_y \\ \phi_x^2 - \|\phi\|^2 \\ -\phi_x \|\phi\|^2 \end{bmatrix} \right) \quad (20)$$

and

$$\frac{\partial \mathbf{w}_i}{\partial \phi_y} = \frac{\partial \mathbf{w}_i}{\partial \mathbf{g}_0} \left(\gamma_c \begin{bmatrix} \phi_x \phi_y \\ -\phi_x \phi_y \\ 0 \end{bmatrix} + \gamma_s \begin{bmatrix} \|\phi\|^2 - \phi_y^2 \\ \phi_x \phi_y \\ -\phi_y \|\phi\|^2 \end{bmatrix} \right), \quad (21)$$

where $\gamma_c = \frac{\gamma \cos(\|\phi\|)}{\|\phi\|^2}$ and $\gamma_s = \frac{\gamma \sin(\|\phi\|)}{\|\phi\|^3}$. The third block of J_i regards the accelerometer bias and is given by:

$$\frac{\partial \mathbf{w}_i}{\partial \mathbf{b}_a} = -J_\pi \mathbf{B}_i \mathbf{R}_{C_i}^\top \quad (22)$$

The fourth block of J_i regards the gyroscope bias and is approximated by:

$$\begin{aligned} \frac{\partial \mathbf{w}_i}{\partial \mathbf{b}_g} \simeq & -J_\pi \mathbf{R}_C^{I^\top} \left([\mathbf{R}_{I_i}^\top \mathbf{m}]_\times \frac{\partial \mathbf{R}_{I_i}}{\partial \mathbf{b}_g} \right. \\ & \left. + \sum_{k=0}^{j-1} \beta_{ki} [\mathbf{R}_{I_i}^\top \mathbf{R}_{I_k} \mathbf{a}_k]_\times \left(\frac{\partial \mathbf{R}_{I_i}}{\partial \mathbf{b}_g} - \frac{\partial \mathbf{R}_{I_k}}{\partial \mathbf{b}_g} \right) \right) \end{aligned} \quad (23)$$

where $[\cdot]_\times$ denotes the skew-symmetric matrix and $\frac{\partial \mathbf{R}_{I_i}}{\partial \mathbf{b}_g}$ is the Jacobian of the rotation w.r.t. the gyroscope bias, approximated by,

$$\frac{\partial \mathbf{R}_{I_i}}{\partial \mathbf{b}_g} \simeq \mathbf{R}_{I_i}^\top \sum_{k=0}^{n_i-1} \mathbf{R}_{I_{k+1}} \Omega_k T_s, \quad (24)$$

where Ω_k is the right Jacobian of SO3 at ω_k ([8], Eq.8). The computation of $\frac{\partial \mathbf{w}_i}{\partial \mathbf{b}_g}$ and $\frac{\partial \mathbf{R}_{I_i}}{\partial \mathbf{b}_g}$ stems from properties of exponential map [8]. The fifth Jacobian that regards the point is simply given by

$$\frac{\partial \mathbf{w}_i}{\partial \mathbf{m}} = J_\pi \mathbf{R}_{C_i}^\top \quad (25)$$

REFERENCES

- [1] A. Bapat, T. Price, and J.-M. Frahm, "Rolling shutter and radial distortion are features for high frame rate multi-camera tracking," in *Proc. CVPR*, 2018.
- [2] C. Campos, J. Montiel, and J. Tardós, "Fast and Robust Initialization for Visual-Inertial SLAM," in *Proc. ICRA*, 2019.
- [3] A. J. Davison, I. D. Reid, N. D. Molton, and O. Stasse, "Monoslam: Real-time single camera slam," *IEEE TPAMI*, vol. 29, no. 6, 2007.
- [4] J. Delmerico and D. Scaramuzza, "A benchmark comparison of monocular visual-inertial odometry," in *Proc. ICRA*, 2018.
- [5] T. Dong-Si and A. I. Mourikis, "Estimator initialization in vision-aided inertial navigation with unknown camera-imu calibration," in *Proc. IROS*, 2012.
- [6] Epic Games, "Unreal Engine," <http://www.unrealengine.com>, 2019.
- [7] G. D. Evangelidis and E. Z. Psarakis, "Parametric image alignment using enhanced correlation coefficient maximization," *IEEE TPAMI*, vol. 30, no. 10, 2008.
- [8] C. Forster, L. Carlone, F. Dellaert, and D. Scaramuzza, "On-manifold preintegration for real-time visual-inertial odometry," *IEEE TRO*, vol. 33, no. 1, pp. 1–21, Feb. 2017.
- [9] G. H. Golub and C. F. van Loan, *Matrix Computations*, 4th ed. JHU Press, 2013.
- [10] R. I. Hartley and A. Zisserman, *Multiple View Geometry in Computer Vision*. Cambridge University Press, 2004.
- [11] J. Hedborg, P.-E. Forssen, M. Felsberg, and E. Ringaby, "Rolling shutter bundle adjustment," in *Proc. CVPR*, 2012.
- [12] W. Huang, H. Liu, and W. Wan, "An online initialization and self-calibration method for stereo visual-inertial odometry," *IEEE TRO*, vol. Preprint, 2020.
- [13] V. Indelman, S. Williams, M. Kaess, and F. Dellaert, "Information fusion in navigation systems via factor graph based incremental smoothing," *Elsevier RAS*, vol. 61, no. 8, pp. 721–738, 2013.
- [14] J. Kaiser, A. Martinelli, F. Fontana, and D. Scaramuzza, "Simultaneous state initialization and gyroscope bias calibration in visual inertial aided navigation," *IEEE RAL*, vol. 2, no. 1, pp. 18–25, 2017.
- [15] L. Kneip, S. Weiss, and R. Siegwart, "Deterministic initialization of metric state estimation filters for loosely-coupled monocular vision-inertial systems," in *Proc. IROS*, 2011.
- [16] S. Leutenegger, S. Lynen, M. Bosse, R. Siegwart, and P. Furgale, "Keyframe-based visual-inertial odometry using nonlinear optimization," *Sage IJRR*, vol. 34, no. 3, pp. 314–334, 2015.
- [17] M. Li and A. I. Mourikis, "Improving the accuracy of ekf-based visual-inertial odometry," in *Proc. ICRA*, 2012.
- [18] Y. Ling, L. Bao, Z. Jie, F. Zhu, Z. Li, S. Tang, Y. Liu, W. Liu, and T. Zhang, "Modeling varying camera-imu time offset in optimization-based visual-inertial odometry," in *Proc. ECCV*, 2018.
- [19] M. L. A. Lourakis and A. A. Argyros, "Is Levenberg-Marquardt the most efficient optimization algorithm for implementing bundle adjustment?" in *Proc. ICCV*, vol. 2, 2005.
- [20] T. Lupton and S. Sukkarieh, "Visual-inertial-aided navigation for high-dynamic motion in built environments without initial conditions," *IEEE TRO*, vol. 28, no. 1, 2012.
- [21] Martinelli, "Vision and imu data fusion: Closed-form solutions for attitude, speed, absolute scale and bias determination," *IEEE TRO*, vol. 28, no. 1, pp. 44–60, Feb. 2012.
- [22] A. Martinelli, "Closed-form solution of visual-inertial structure from motion," *Springer IJCV*, Aug. 2013.
- [23] A. I. Mourikis and S. I. Roumeliotis, "A multi-state constraint kalman filter for vision-aided inertial navigation," in *Proc. ICRA*, 2007.
- [24] R. Mur-Artal, J. Montiel, and J. D. Tardós, "Orb-slam: a versatile and accurate monocular slam system," *IEEE TRO*, vol. 31, no. 5, pp. 1147–1163, 2015.
- [25] R. Mur-Artal and J. D. Tardós, "Visual-inertial monocular slam with map reuse," *IEEE Robotics and Automation Letters*, vol. 2, no. 2, 2017.
- [26] D. Nistér, O. Naroditsky, and J. R. Bergen, "Visual odometry," in *Proc. CVPR*, 2005.
- [27] T. Qin and S. Shen, "Robust initialization of monocular visual-inertial estimation on aerial robots," in *Proc. IROS*, 2017.
- [28] E. Rosten, R. Porter, and T. Drummond, "FASTER and better: A machine learning approach to corner detection," *IEEE TPAMI*, vol. 32, pp. 105–119, 2010.